Aerospace Science and Technology 177 (2026) 112842

Contents lists available at ScienceDirect

Aerospace Science and Technology

journal homepage: www.elsevier.com/locate/aescte

Continuous parameterisation of wing movable layout for optimisation

Stefan de Boer *, Roeland De Breuker, Jurij Sodja

Delft University of Technology, Kluyverweg 1, Delft, 2629HS, The Netherlands

A R T I C L E I N F O

Communicated by Dr Mehdi Ghoreyshi

Keywords:
Movables
Doublet lattice method
B-spline
Aeroelasticity
Parameterisation

A B S T R A C T

This paper presents a novel methodology for continuous parameterisation of movables, which takes advantage of the ability of the doublet lattice method to describe aerodynamic forces using downwash. The movables are described in the continuous space using a downwash distribution generated using a B-spline surface. The parameterisation allows for any number of control surfaces to be positioned along the trailing edge of the wing. A high aspect ratio strut-braced wing aircraft model has been used to determine the handling qualities and manoeuvre load alleviation performance at different flight conditions, demonstrating and assessing the methodology for modelling movables distributions. The results in the paper demonstrated a successful application of a novel continuous movable parameterisation methodology, which can be applied to an aircraft for which only the planform and initial structural parameters are known. Furthermore, the results obtained with the continuous parameterisation advocate for the use of movables which can change their shape in the spanwise direction.

1. Introduction

The drive for greater fuel efficiency and reduced emissions is pushing modern aircraft toward lighter, more flexible wing designs. Such flexibility introduces strong aerodynamic–structural interactions that can degrade performance if not properly managed. Active control systems address this challenge by dynamically adjusting wing movables to achieve optimal aerodynamic shapes, thereby improving control, reducing drag, alleviating structural loads, and enhancing performance across the flight envelope [1].

Several studies explored the use of active control for performance enhancements. Examples are the works by Sanghi et al. [2–4] who investigated the influence of the position of leading edge (LE) and trailing edge (TE) movables. Another example is Wunderlich and Siebert [5] who investigated the usage of the TE movables to improve cruise flight performance to find a fuel burn reduction ranging between 0.5 % to 1.7 % depending on the flight conditions. The works by Riso et al. [6] and Ma et al. [7] focused on the influence of aileron positioning on aircraft handling qualities (HQ). Considering active load control, Muradas et al. [8,9] optimised the position of an aileron deflected to 15° and wing structure for manoeuvre load alleviation (MLA) considering HQs to find a 3 % load reduction compared to the reference, while Pusch et al. [10] investigated the optimal position of two ailerons for gust load alleviation (GLA) considering HQs using control co-design to find a 9 % reduction in root bending moment (RBM) compared to a wing with the reference aileron positions.

The works discussed above parameterised the movables in a discrete fashion by specifying the spanwise extend of each movable. This methodology is similar to industrial movable sizing processes as shown by Reckzeh [11]. Furthermore, the chord of the movable is also a design variable, which is especially important for the high lift devices (HLDs) [12]. However, the available chord fraction is generally limited by the internal wing structure [9,10].

Furthermore, the works presented above improved the aircraft's performance at one flight point. On the other hand, Handojo et al. [13–15] considered multiple different flight points during the structural and control co-design optimisation for MLA and GLA using a fixed movable layout. Similar work was also performed by Binder et al. [16], who sized the structure using a fixed movable layout and investigated the effect of simultaneously applying active control and structural sizing. Binder et al. [16] found that the largest reduction in mass could be achieved through the application of MLA, with the addition of structural tailoring and GLA providing further mass reductions. The work by Bona and Risse [17] has shown a collaborative approach to sizing the wing and its movables, considering different flight points along a mission trajectory. However, they considered load alleviation as a secondary function of the movable system, which, as shown by Binder et al. [16], can lead to suboptimal use of the movables.

When considering flight conditions at the design point, the flexibility can be accounted through aeroelastic tailoring or active control. However, the wing cannot be fully optimised for the entire flight envelope because of conflicting structural and control requirements [18,19].

* Corresponding author.
E-mail addresses: s.deboer-2@tudelft.nl (S. de Boer), r.debreuker@tudelft.nl (R. De Breuker), j.sodja@tudelft.nl (J. Sodja).

https://doi.org/10.1016/j.ast.2026.112842
Received 6 February 2026; Received in revised form 29 May 2026; Accepted 7 June 2026
Available online 11 June 2026

List of Symbols

Symbol	Description/Units
AIC	aerodynamic influence coefficient matrix
c	chord [m]
C_{AoA}	angle of attack constraint
C_{defl}	downwash constraint
C_{η}	elevator deflection angle constraint
C_i	constraint
C_L	lift coefficient
C_{loads}	limit load constraint
c_{mov}	chordwise fraction of movable region
C_p	roll rate constraint
c_{ref}	reference chord [m]
$\mathbf{D}_{\mathrm{CP}}$	downwash values at the control points
$\mathbf{D}^i_{jk}$	differentiation matrices
f	ratio of bending moment
F_z	shear force [N]
j	downwash collocation point
k	box reference point
l	load acting point
M	number of spanwise panels in the movable region
M_{β}	hinge moment [Nm]
$M_{\beta,\mathrm{all}}$	total hinge moment [Nm]
$M_{\beta,\mathrm{MLA}}$	hinge moment during MLA [Nm]
$M_{\beta,\mathrm{roll}}$	hinge moment during roll [Nm]
M_x	bending moment [Nm]
$M^{\mathrm{clean}}_{x,c}$	bending moment at location c for a clean wing [Nm]
$M^{\mathrm{MLA}}_{x,c}$	bending moment at location c during MLA [Nm]
N	number of chordwise panels in the movable region
$N_{i,p}(x)$, $N_{l,q}(y)$	B-spline basis functions of degree p and q
n_z	load factor
$\mathbf{P}_{i,l}$	B-spline control points
$\mathbf{P}^{\mathrm{a}}_k$	total aerodynamic forces [N]
$\mathbf{P}^{\mathrm{a,\,g}}_k$	gust aerodynamic force [N]
$\mathbf{P}^{\mathrm{a,\,s}}_k$	steady aerodynamic forces [N]
$\mathbf{P}^{\mathrm{a,\,us}}_k$	unsteady aerodynamic forces [N]
$\mathbf{P}_{c,\mathrm{l}}$, $\mathbf{P}_{c,\mathrm{u}}$	limit loads [N, Nm]
p_{max}	maximum achievable steady-state roll rate [°/s]
q	pitch rate [°/s]
q_{∞}	free-stream dynamic pressure [Pa]
r	moment arm [m]
s	Laplace variable
$\mathbf{S}_{kj}$	aerodynamic integration matrix
U_{∞}	free-stream velocity [m/s]
V_i	objective function
$\mathbf{v}_j$	flow component normal to the panels [m/s]
$\mathbf{w}_j$	downwash vector [m/s]
$\mathrm{w}_{j,\mathrm{ail}}$	aileron downwash [m/s]
$\mathbf{w}_{j,\mathrm{cam}}$	downwash due to camber and twist of the aerofoils [m/s]
$\mathbf{w}_{j,\mathrm{cs}}$	downwash due to control surface deflection [m/s]
$\mathrm{w}_{j,\mathrm{f}}$	flap downwash [m/s]
$\mathrm{w}_{j,\mathrm{fn}}$	flaperon downwash [m/s]
$\mathbf{w}_{j,\mathrm{rbm}}$	downwash due to rigid body motion [m/s]
$\mathbf{w}_{j,\dot{\mathrm{u}}\mathrm{f}}$	downwash due to flexible structural motion [m/s]
$\mathbf{w}_{j,\mathrm{uf}}$	downwash due to flexible structural deformations [m/s]
x_i	knots of B-spline
$\mathbf{X}$	knot vector
$\mathbf{Y}$	knot vector
y_l	knots of B-spline
y_1	spanwise start position [m]
y_2	spanwise stop position [m]
Γ_j	circulation strength [m^2/s]
δ	control surface deflection [°]
$\Delta\mathbf{c}_{\mathrm{p}}$	complex differential pressure coefficient
$\Delta\mathrm{y}_{\mathrm{cp}}$	spanwise B-spline control point spacing [m]
ε	control effectiveness
η	elevator deflection [°]
ξ	aileron deflection [°]
$\mathbf{\Phi}_{kx}$	movable mapping matrix

List of Acronyms

Acronyms	Description
AoA	angle of attack
CFD	computational fluid dynamics
DLM	doublet lattice method
GLA	gust load alleviation
HLD	high lift device
HQ	handling qualities
HTP	horizontal tailplane
LE	leading edge
MLA	manoeuvre load alleviation
MTOW	maximum take-off weight
PrP	Prandtl-Plane
RANS	Reynolds-averaged Navier-Stokes
RBM	root bending moment
RFA	rational function approximation
SLSQP	sequential least squares programming
TE	trailing edge
TRIC	translation induced camber
UHARW	ultra high aspect ratio wing
UVLM	unsteady vortex lattice method
VCCTEF	variable camber continuous trailing edge flap
VLM	vortex lattice method
XDSM	extended design structure matrix

Therefore, instead of resisting the flexibility of the aircraft structure, embracing it and changing the wing shape actively over the whole flight envelope using continuous movables would be more natural, such that the performance gap between the optimal configuration and the current cruise configuration can be reduced [20].

Continuous movables can be split into two main groups. The first group compromises morphing concepts, such as NASA's variable camber continuous trailing edge flap (VCCTEF) concept [21–23] and TU Delft's translation induced camber (TRIC) concept [19,20,24,25]. These systems continuously modify their shape in both the spanwise and chordwise directions, providing high flexibility for drag minimisation, load alleviation, and shape control. The second group are distributed discrete movables which only degree of freedom is the deflection angle, but are positioned along the trailing edge (TE) in multiple section. Examples of the application of these distributed discrete movables are the works by Stanford [26,27], who investigated their use for load alleviation and flutter suppression, and found a trade-off between mass of the movable system and the structural mass.

The mentioned works considered wings with internal fuel storage, which limits the design space available to the wing movables. The use of novel fuels, such as hydrogen, creates dry wings, because of the high pressure storage requirements [28]. The absence of wing fuel tanks expands the available structural and geometric design space for trailing-edge movables, offering new opportunities for aerodynamic and load optimisation. To efficiently explore this enlarged design space, a method capable of representing both conventional discrete and continuously deformable movables is required.

Despite significant research on active control being performed, no existing framework allows for the representation of continuous and discrete movables for the exploration of the enlarged design space. This paper addresses this gap through the introduction of a novel B-spline based parameterisation methodology that allows for the continuous representation of TE movables in the chordwise and spanwise directions. Instead of optimising movable deflection, the B-spline based parameterisation directly optimises the downwash distribution associated with the movables. This approach allows the number of movables to be defined during post-processing rather than predetermined during optimisation, thereby providing a flexible and scalable framework for performance and load optimisation.

To demonstrate the proposed methodology, an ultra-high aspect ratio strut-braced wing aircraft is used as a test case. The method's capability is assessed by evaluating handling qualitiess (HQs) and manoeuvre load alleviation (MLA) performance across multiple flight points, demonstrating its ability to simultaneously consider varying conditions.

The remainder of this paper is structured as follows. Section 2 introduces the aerodynamic modelling and the novel continuous parameterisation methodology. Section 3 presents the optimisation framework, while Section 4 defines the design problem. Results are presented and discussed in Section 5, after which the key findings and concluding remarks are given in Section 6.

2. Continuous movable description

This section discusses a novel parameterisation methodology proposed to model the movables. First, the aerodynamic modelling approach is presented, followed by an explanation of the continuous parameterisation methodology. The section closes with a discussion on the estimation of the hinge moment, which is used as an indicator of the movable system mass, as the higher the hinge moment, the larger the movable system mass becomes.

2.1. Aerodynamic modelling of movables

Several different methods are available to model movable aerodynamics, such as empirical listings of the lift and moment coefficients for a known movable deflection angle [29,30], the unsteady vortex lattice method (UVLM) [31,32], the doublet lattice method (DLM) [10,33], or the use of computational fluid dynamics (CFD) [34,35].

All of the methods listed have different pros and cons. For example, the empirical listing is very fast but only works after estimating the required movable surface area and the corresponding aerodynamic coefficients as a function of control surface deflection [29]. In contrast, CFD simulations allow for different movable sizes and include nonlinear flow effects such as flow separation, but they are computationally expensive. One can include the nonlinear flow effects through the use of empirical methods, but this is only available for a limited set of movable sizes and deflections [29,30]. Finally, UVLM and DLM can model movables of different sizes, but neither of them can account for flow separation.

In the end, DLM was chosen as it determines the aerodynamic forces using downwash. Fig. 1 shows the discretisation of the aircraft lifting surfaces using trapezoidal panels. The aerodynamic force generated by the downwash is acting at load acting point, l, which is located at the quarter chord of the panel. The downwash is applied at downwash collocation point, j, which is located at the three-quarter chord point [36]. Finally, Fig. 1 shows the box reference point, k, located at the panel's mid-chord. The movement of k determines the required induced downwash.

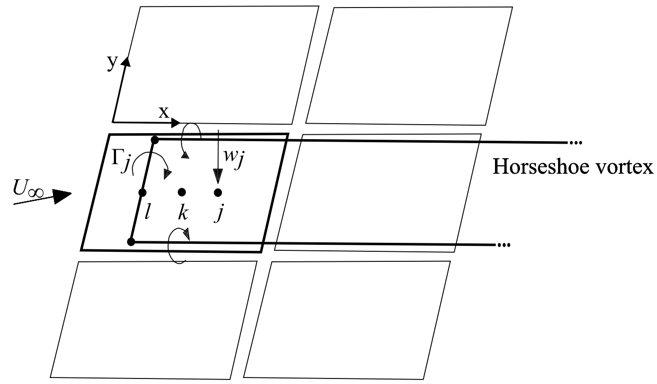

Fig. 1. Geometrical DLM mesh with different points (l, k, j). Adapted from Voß [33].

For quasi-steady aerodynamics the solution of DLM is equivalent to vortex lattice method (VLM) [33,36–38]. Hence, the derivation given by Katz and Plotkin [39] can be followed.

By applying the flow tangency condition at j, the flow component normal to the panels, $\mathbf{v}_j$, can be determined, which is normalised by the free-stream velocity, U_∞, to create the downwash vector, $\mathbf{w}_j$, as shown in Eq. (1) [10,33].

$$\mathbf{w}_j = \frac{\mathbf{v}_j}{U_\infty} \tag{1}$$

Combining Eq. (1) with the aerodynamic influence coefficient matrix, **AIC**, which relates $\mathbf{w}_j$ to the circulation strength, Γ_j, on each panel, leads to the complex differential pressure coefficient, $\Delta\mathbf{c}_\mathrm{p}$, described as follows [36].

$$\Delta\mathbf{c}_\mathrm{p} = \mathbf{AIC}\mathbf{w}_j \tag{2}$$

The $\Delta\mathbf{c}_\mathrm{p}$ allows for the determination of the lift vector at l. To map the effect of the $\mathbf{w}_j$ to the lift vector at k, the aerodynamic integration matrix, $\mathbf{S}_{kj}$, is used. Combining $\mathbf{w}_j$, $\mathbf{S}_{kj}$, the **AIC**, and the free-stream dynamic pressure, q_∞, allows for the determination of the steady aerodynamic forces, $\mathbf{P}_k^{\mathrm{a,\,s}}$, as follows [33,36]:

$$\mathbf{P}_k^{\mathrm{a,\,s}} = q_\infty \mathbf{S}_{kj}\mathbf{AIC}^{\mathrm{steady}}\left(\mathbf{w}_{j,\mathrm{rbm}} + \mathbf{w}_{j,\mathrm{cs}} + \mathbf{w}_{j,\mathrm{uf}} + \mathbf{w}_{j,\dot{\mathrm{u}}\mathrm{f}} + \mathbf{w}_{j,\mathrm{cam}}\right). \tag{3}$$

To determine the total steady aerodynamic force at each panel, described using $\mathbf{P}_k^{\mathrm{a,\,s}}$, different steady downwash sources must be considered. These sources are due to the rigid body motion, $\mathbf{w}_{j,\mathrm{rbm}}$, the flexible deformation, $\mathbf{w}_{j,\mathrm{uf}}$, the flexible motion, $\mathbf{w}_{j,\dot{\mathrm{u}}\mathrm{f}}$, the control surface deflection, $\mathbf{w}_{j,\mathrm{cs}}$, and the aerofoil camber, $\mathbf{w}_{j,\mathrm{cam}}$.

$\mathbf{P}_k^{\mathrm{a,\,s}}$ enables the trimming of the aircraft and the calculation of loads for manoeuvres such as pull-up, push-down, or roll. To be able to perform gust analyses both the gust aerodynamic force, $\mathbf{P}_k^{\mathrm{a,\,g}}$ and unsteady aerodynamic forces, $\mathbf{P}_k^{\mathrm{a,\,us}}$ need to be added to the steady aerodynamic forces to get the total aerodynamic forces, $\mathbf{P}_k^{\mathrm{a}}$, seen by the aircraft:

$$\mathbf{P}_k^{\mathrm{a}} = \mathbf{P}_k^{\mathrm{a,\,s}} + \mathbf{P}_k^{\mathrm{a,\,g}} + \mathbf{P}_k^{\mathrm{a,\,us}}. \tag{4}$$

The forces associated with $\mathbf{P}_k^{\mathrm{a,\,g}}$ are determined using the gust properties as described in CS25 [40]. The $\mathbf{P}_k^{\mathrm{a,\,us}}$ component is necessary to allow for the inclusion of unsteady aerodynamic characteristics associated with short and sudden events, such as a gust encounter. These forces are determined in the frequency domain, but to obtain the unsteady forces in the time domain, the rational function approximation (RFA) is used [33,37].

Through the summation in Eq. (4), the steady and unsteady components of the downwash sources presented in Eq. (3), as well as additional terms related to the gust encounter, are accounted for. Hence, the total aerodynamics can be described as

$$\mathbf{P}_k^{\mathrm{a}} = q_\infty \mathbf{S}_{kj}\mathbf{AIC}\mathbf{w}_j. \tag{5}$$

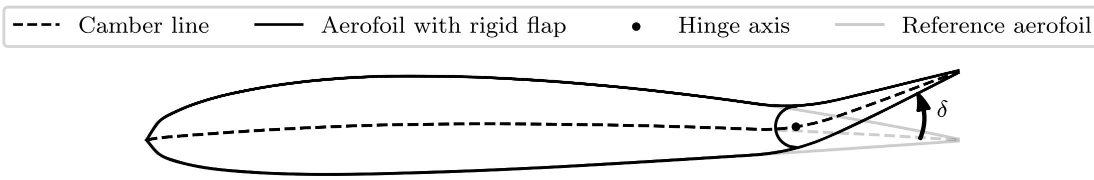

(a) Aerofoil with rigid movable.

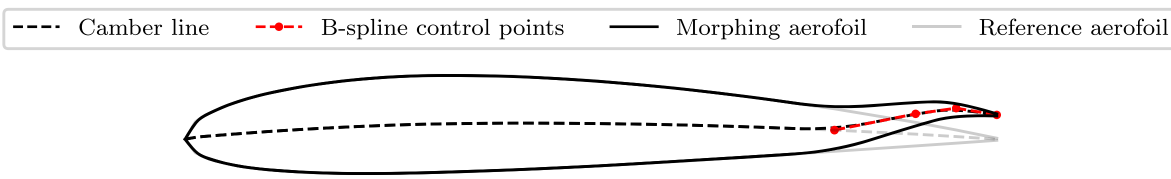

(b) Modelling movable by changing camber line.

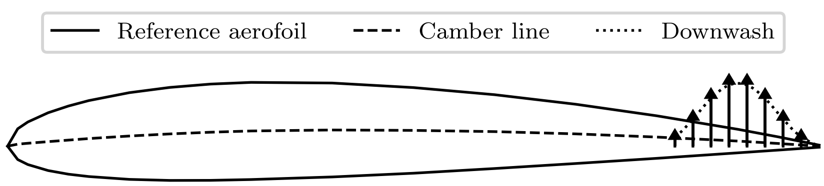

(c) Modelling movable using $\mathbf{w}_j$. Arrows indicate $\mathbf{w}_j$ magnitude.

Fig. 2. Different methodologies to model movables.

Eqs. (3) to (5) show that the interesting component for movable allocation is

$$\mathbf{P}_k^{\text{a, cs}} = q_\infty \mathbf{S}_{kj}\mathbf{AIC}\mathbf{w}_{j,\text{cs}}. \tag{6}$$

As both the $\mathbf{S}_{kj}$ and the **AIC** are functions of the panel discretisation applied to the aircraft, they can be considered constant. In contrast, downwash due to control surface deflection, $\mathbf{w}_{j,\text{cs}}$ is a parameter that can be assigned to every panel individually.

For rigid movables, the downwash due to their deflection is determined as follows. As shown by the example in Fig. 2a, all DLM panels associated with the movable get assigned a $\mathbf{w}_{j,\text{cs}}$ that is dependent on control surface deflection, δ, with the downwash value being calculated using

$$\mathbf{w}_{j,\text{cs}} = \left(\mathbf{D}^1_{jk} + s\frac{c_{\text{ref}}/2}{U_\infty}\mathbf{D}^2_{jk}\right)\boldsymbol{\Phi}_{kx}\delta. \tag{7}$$

In this equation, the differentiation matrices, $\mathbf{D}^i_{jk}$, are used to transform the panel velocities and displacements from the reference point at k to a downwash at j. $\mathbf{D}^1_{jk}$ relates the steady rotation to the $\mathbf{w}_{j,\text{cs}}$, whereas $\mathbf{D}^2_{jk}$ does this for the unsteady rotation [10,36]. The remaining variables in Eq. (7) are the Laplace variable, s, the reference chord, c_{ref}, the free-stream velocity, U_∞, and movable mapping matrix, $\boldsymbol{\Phi}_{kx}$ [10].

2.2. Continuous movable modelling

Using continuous movables, such as morphing concepts, or distributed discrete movables, allows for the creation of the optimal wing shape for different flight points [18,19,41]. However, morphing movables do not necessarily have a constant δ around their hinge axis, as can be seen when comparing Fig. 2a and b, therefore the movable modelling methodology described in Eq. (7) can not be used anymore.

One method to describe continuous movables is the use of B-splines to provide a smooth description of the different geometric shapes. An example of this method is shown in Fig. 2b, where the B-spline describes the morphed the camber line, which in turn influences the outer mould line. In contrast, the proposed methodology directly describes the movable's downwash in the continuous space using B-spline surfaces. An example of the downwash application is shown in Fig. 2c.

The downwash distribution is defined using:

$$\mathbf{w}^{\text{cs}}(x,y) = \sum_{i=0}^{m}\sum_{l=0}^{n} N_{i,p}(x)N_{l,q}(y)\mathbf{p}_{i,l}, \tag{8}$$

which uses the B-spline control points, $\mathbf{p}_{i,l}$, and the B-spline basis functions of degree p and q, $N_{i,p}(x), N_{l,q}(y)$, that are generated using the

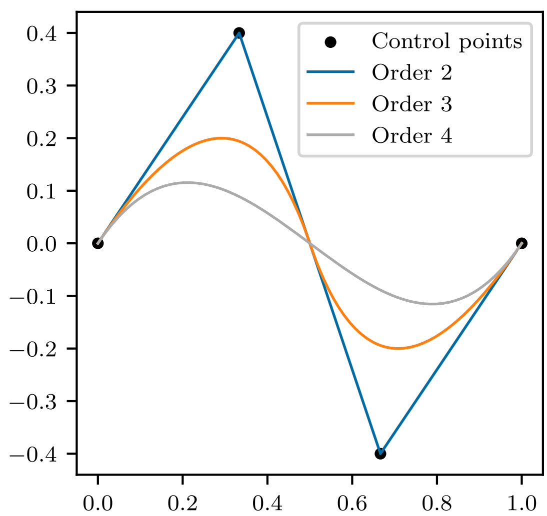

Fig. 3. Effect of curve order on B-spline behaviour.

Cox-de Boor recursion formula [42]:

$$N_{i,0}(x) = \begin{cases} 1 & \text{if} \quad x_i \leq x < x_{i+1} \\ 0 & \text{otherwise} \end{cases} \tag{9a}$$

$$N_{i,p}(x) = \frac{x - x_i}{x_{i+p} - x_i} N_{i,p-1}(x) + \frac{x_{i+p+1} - x}{x_{i+p+1} - x_{i+1}} N_{i+1,p+1}(x) \tag{9b}$$

where x_i are the knots inside the knot vector $\mathbf{X}$, which are a set of parameters that determine how and where the control points influence the B-spline curve. For the basis function $N_{l,q}(y)$ used in Eq. (8), the procedure shown in Eqs. (9a) and 9b is also followed. However, in this case, the x_i are replaced with the y_l from the knot vector $\mathbf{Y}$, and the degree q is used.

To ensure that the Cox-de Boor recursion formula can be used, the number of control points must be equal to or greater than the order of the curve [42]. Furthermore, the degrees p and q are one less than the order of the curve. Hence, the minimum number of control points is degree + 1.

To model the reflex behaviour presented in Fig. 2b using the downwash distribution, Fig. 3 shows that four chordwise control points are necessary to model the positive and negative downwash seen by the reflex movable. Furthermore, to create a smooth changing distribution, which is not piecewise linear, the degree of p and q must be at least two, with the B-spline being of order three. Fig. 3 furthermore shows that a higher-order B-spline reduces the effect of the control points, meaning the required reflex behaviour cannot be modelled without adding more control points. Hence, the decision was taken to use the second-degree basis functions, with the corresponding B-spline being of order three.

To determine the downwash distribution, the $\mathbf{p}_{i,l}$ are distributed over the wing. The $\mathbf{p}_{i,l}$ and knots are distributed inside the movable region, whose parameterisation is indicated in Fig. 4. The parameterisation consists of spanwise start position, y_1, the spanwise stop position, y_2, the chordwise fraction of movable region, c_{mov}, expressible as a fraction of the chord, c, and the spanwise B-spline control point spacing, Δy_{cp}. These are user defined variables that allow for the inclusion of positional constraints, that are, for example, given by the wing structure. Within the movable regions, the downwash values at the control points, $\mathbf{D}_{\text{CP}}$ is specified, from which the movable position can be determined.

To allow for the different types of movable functions, such as ailerons or flaps, a flaperon is created. It is modelled using two overlapping downwash surfaces. Fig. 5 shows the downwash contributions of the flap surface in blue and the aileron surface in red. The total movable contribution, indicated in black, is determined by summing the two downwash surfaces and applying these to the DLM mesh by evaluating the downwash distribution at the collocation point of each panel:

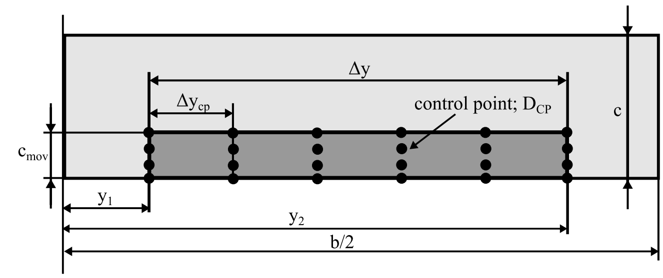

Fig. 4. Parameterisation of the movable regions. Light gray: wing; Dark gray: movable region.

$$\mathbf{w}_{j,\text{cs}} = \mathbf{w}^{\text{cs}}(x_j, y_j). \tag{10}$$

2.3. Hinge moment determination

To perform a trade-off between movable size and the corresponding movable loads on the optimisation objective, a parameter that describes the effect of the movable size and motion on the mass of the movable system needs to be considered. The parameter is necessary to prevent the trivial solution of the bigger the movable, the larger the load alleviation capability. This paper proposes the hinge moment as a parameter to evaluate the effect of different movable sizes, with a larger hinge moment requiring larger actuators, leading to an increased movable system mass. This parameter has been inspired by the work of De Breuker and Werter [43], who developed a methodology to determine the mass of a morphing movable system.

In this case, the magnitude and location of the aerodynamic force on each DLM panel is used to represent the movable system mass. Using the location of each panel associated with the movable and the position of the hinge axis, the moment arm, r, can be determined. Using the parameters indicated in Fig. 6, the hinge moment, M_β, at spanwise position, j is calculated as follows:

$$M_{\beta j} = \sum_{i=0}^{N} |P_{k,i}| r_i \tag{11}$$

where N is the number of chordwise panels in the movable region.

To get the hinge moment of the whole movable system, $M_{\beta j}$ is summed over the whole movable region

$$M_\beta = \sum_{j=0}^{j=M} |M_{\beta j}| = \sum_{j=0}^{j=M} \left| \sum_{i=0}^{N} P_{k,i} r_i \right| \tag{12}$$

with the number of spanwise panels in the movable region indicated using M. In Eq. (12), the absolute value of $M_{\beta j}$ is used to prevent neighbouring spanwise positions with different $M_{\beta j}$ bringing the total M_β value to zero. This is necessary, as to create a region with $M_{\beta j}$ values of opposite signs, the movable system still needs actuators, which influence the movable system mass.

3. Downwash optimisation framework

An optimisation framework was created to apply the proposed movable parameterisation. The XDSM [44] illustrating the general layout and corresponding dataflow is shown in Fig. 7.

The framework, created using openMDAO [45], consists of two loops. The inner loop optimises the downwash distribution for the HQ constraints. The results from this loop are passed as a set of constraints to the outer loop, which performs the MLA optimisation. Each loop uses the sequential least squares programming (SLSQP) algorithm included in the openMDAO ScipyOptimizeDriver [45] to perform the optimisation.

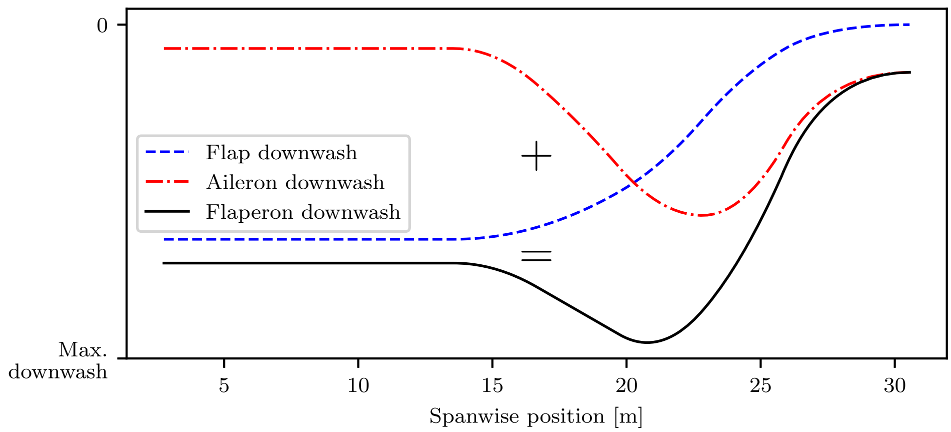

Fig. 5. Downwash contributions to flaperon. Blue: Flap-like behaviour; Red: Aileron-like behaviour; Black: Flaperon behaviour.

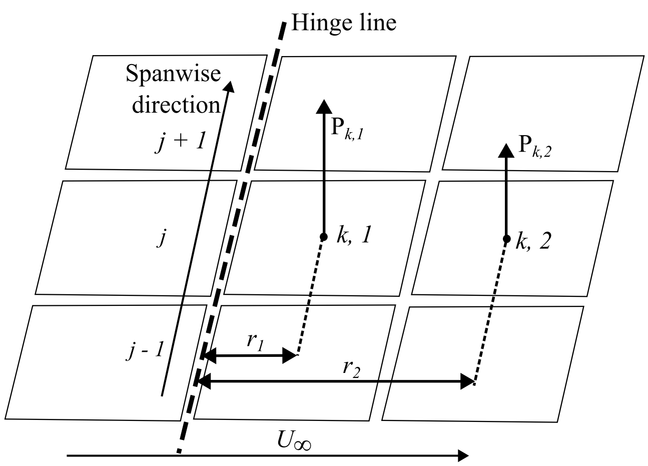

Fig. 6. Movable region used for hinge moment determination.

The B-splines are generated using the NURBS-Python package developed by Bingol and Krishnamurthy [46], which is used inside the optimisation loops. The downwash distribution is mapped to the DLM panels using Eq. (10), with the corresponding downwash at each DLM panel serving as an input for the aeroelastic analysis.

For the aeroelastic analysis, the open-source code LoadsKernel is used. LoadsKernel has been developed at DLR Institute of Aeroelasticity, and allows for the calculation of quasi-steady and dynamic manoeuvre loads, unsteady gust loads in the time and frequency domain, and dynamic landing loads based on a generic landing gear module. The quasi-steady and unsteady aerodynamics are modelled using DLM, with the structural behaviour modelled using a modal representation of the structure, that is obtained through a modal analysis [33,37].

4. Design problem formulation

The following section presents the design problem. First, the aircraft model and flight points are discussed, followed by the definition of the movable regions. To close the section, the optimisation problem is formulated.

4.1. Aircraft model

The aircraft model used throughout the analysis is a strut-braced, hydrogen-fueled ultra high aspect ratio wing (UHARW) aircraft, with a passenger capacity and range similar to typical single-aisle aircraft. The model has been created by ONERA during the UPWING project[1] [47]. An overview of the model is shown in Fig. 8, which illustrates the structure in blue, the DLM panels in grey, and the red dots indicate some of the locations of load extraction for visualisation purposes. The aircraft properties are listed in Table. 1. As can be seen in Fig. 8, the DLM panels are only applied to the wing and tail.

Table 1
Aircraft parameters [47].

Parameter	Value
Span	62 m
Length	50 m
Aspect Ratio	25
Wing Sweep at quarter chord	26.2°
Number of DLM panels	1840
Strut attachment location	50 % semispan, 50 % chordwise

Table 2
Flight points considered during optimisation.

Mach number	Altitude [m]	Dynamic pressure [kPa]
0.20	0.0	2.8
0.30	152.4	6.3
0.40	1524.0	9.4
0.45	3048.0	9.9
0.55	4572.0	12.1
0.60	6096.0	11.7
0.69	7620.0	12.5
0.78	9144.0	12.8
0.78	11 277.6	9.2

The shear force, bending and torsional loads are extracted at 31 equally distributed cross-sections in each wing half. Only the right wing is considered for symmetric manoeuvres, since the loading is symmetrical on the aircraft. In contrast, the loads are extracted on the left and right wings during rolling manoeuvres.

During the optimisation process, different flight points are considered, which are presented in Table. 2. The considered the flight points range from low-speed approach to cruise conditions. The mass of the aircraft was set at maximum take-off weight (MTOW) for all flight points. Because the aircraft is fuelled using hydrogen, the non structural mass of the aircraft is centred within the fuselage, and hence, has a minimal impact on the roll intertia of the aircraft.

[1] https://www.clean-aviation.eu/research-and-innovation/clean-aviation/clean-aviation-projects/up-wing

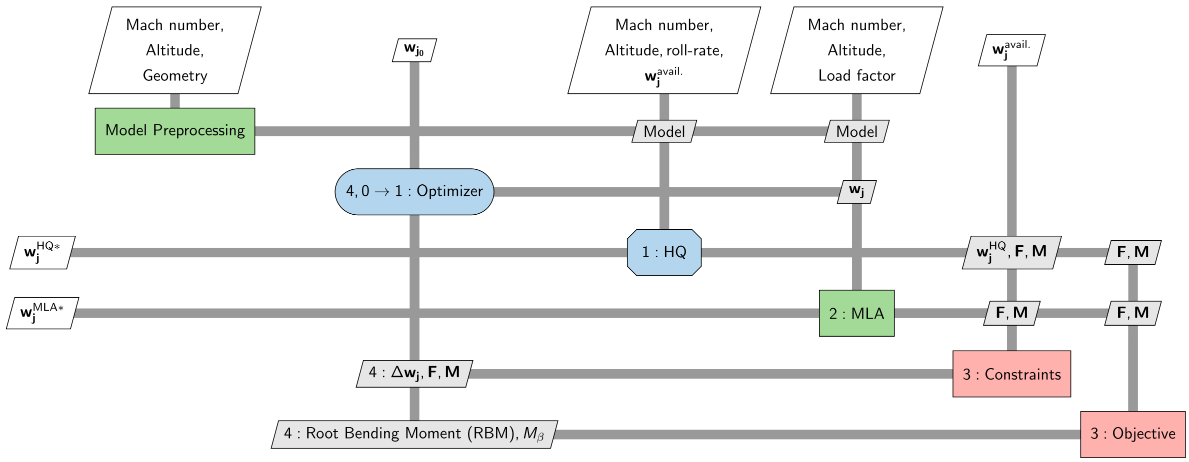

Fig. 7. XDSM for downwash optimisation for HQ and MLA.

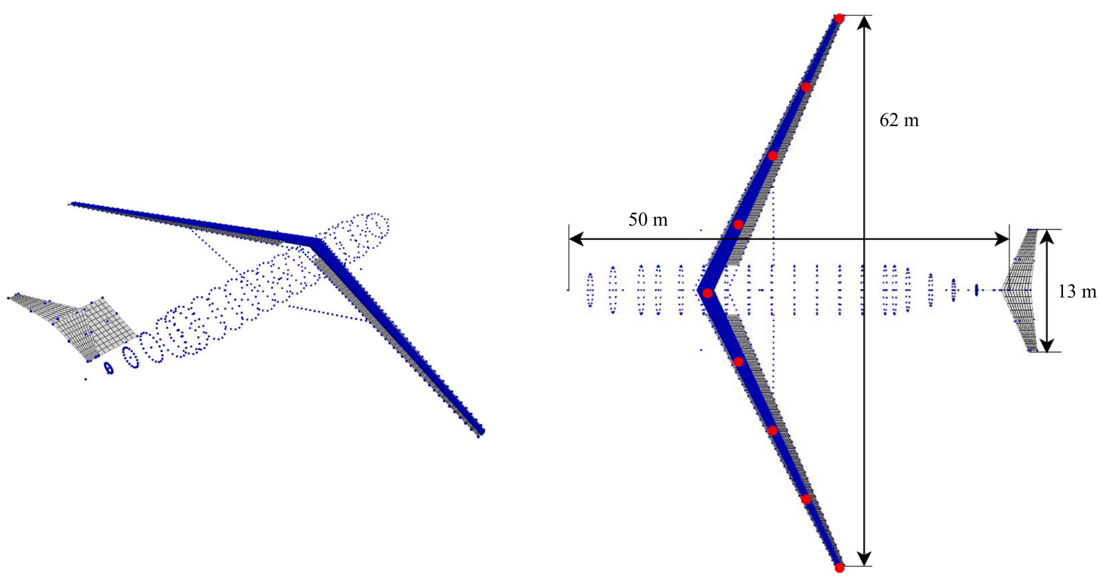

(a) Isometric view of aircraft model. (b) Basic dimensions of aircraft model.

Fig. 8. Aircraft model [47]. The structure is blue, the DLM mesh is grey, and the red dots indicate load extraction points. (For interpretation of the references to colour in this figure legend, the reader is referred to the web version of this article).

Table 3
Movable region parameters.

Parameter	Value
y_1	0 % semi-span
y_2	100 % semi-span
c_{mov}	0.2 c
Δy_{cp}	3 m

The geometric definition for the movable regions used throughout the optimisation is presented in Table. 3. The parameters correspond to the parameterisation presented in Fig. 4.

4.2. Objective function

In this paper, the objective function, V_i, consists of two components. The first component allows for the inclusion of the movable system weight estimation through the consideration of M_β, with the second objective being related to the reduction of wing loads during pull-up manoeuvres.

The first objective is the M_β during roll and MLA, which is defined as:

$$V_1 : M_{\beta,\text{all}} = M_{\beta,\text{roll}} + M_{\beta,\text{MLA}} \tag{13}$$

where the hinge moment during roll, $M_{\beta,\text{roll}}$, is summed with hinge moment during MLA, $M_{\beta,\text{MLA}}$, to create the total hinge moment, $M_{\beta,\text{all}}$.

Table 4
Constraint overview.

ID	Value
C_{loads}	$\mathbf{P}_{c,1} \leq \mathbf{P}_c \leq \mathbf{P}_{c,u}$
C_{defl}	$\begin{cases} 0 \leq w_{j,f} \leq 0.55 \\ -0.4 \leq w_{j,\text{ail}} \leq 0.4 \\ -0.4 \leq w_{j,\text{fn}} \leq 0.55 \end{cases}$
C_p	$p \geq 15\,°/\text{s}$
C_{AoA}	$-10° \leq \text{AoA} \leq 10°$
C_η	$-15° \leq \eta \leq 15°$

The different hinge moments for the HQ and MLA components are determined using the methodology described in Section 2.3.

The second objective is to alleviate the wing loads during a pull-up manoeuvre. The goal for MLA is to reduce the wing bending moment seen during the manoeuvres. Hence, the objective function is defined as:

$$V_2: \ f = \frac{M_{x,c}^{\text{MLA}}}{M_{x,c}^{\text{clean}}} \tag{14}$$

where the ratio of bending moment, f, is minimised. To determine f, the bending moment at location c during MLA, $M_{x,c}^{\text{MLA}}$, and the bending moment at location c for a clean wing, $M_{x,c}^{\text{clean}}$, are necessary. Throughout this paper, the root bending moment (RBM) is used for the determination of f, as this is one of the main drivers behind wing structural weight [10,48].

To create the multi-objective optimisation objective, the objective in Eq. (13) is scaled, after which both objectives are summed together with equal weights. For the scaling of Eq. (13), the maximum achievable M_β is used. Whereas for Eq. (14), the scaling was performed when f was determined. Hence, the multi-objective optimisation considers both the movable system weight and RBM reduction as equal contributors during the optimisation.

4.3. Optimisation problem formulation

The overall optimisation problem considered can be formulated as

$$\min_{\mathbf{D}_{\text{CP}}}\left(V_i\right) \quad \text{such that} \quad C_{\text{loads}} \dots C_\eta \quad \text{are satisfied.} \tag{15}$$

where the V_i is described in Section 4.2, An overview of the constraints, C_i, is given in Table. 4, with a detailed description of each constraint presented below. The design variables are $\mathbf{D}_{\text{CP}}$, which are discussed in Section 2.2.

Throughout the optimisation, five constraints are considered. The first is the limit load constraint, C_{loads}, which is related to the limit loads seen by the aircraft during a manoeuvre. It ensures that the aircraft's structural limit loads are not exceeded during the application of downwash. The second is the downwash constraint, C_{defl}, which limits the downwash value at the control points. It is necessary because DLM overestimated the authority of the movable, as it cannot account for flow separation. The roll rate constraint, C_p, ensures that the lateral manoeuvrability specified by regulations is achieved. The final two constraints are the angle of attack constraint, C_{AoA}, and elevator deflection angle constraint, C_η, which are also necessary because DLM cannot model flow separation, hence, no stall occurs.

To determine the limit loads, $\mathbf{P}_{c,1}, \mathbf{P}_{c,u}$, extreme manoeuvres are simulated using representative steady trim cases performed on the aircraft without any wing movables. The subscript c indicates cirital load locations, examples of which are the bending moment, M_x, and shear force, F_z, at the wing root. An overview of the manoeuvres used to compute the limit loads, which have been inspired by Pusch et al. [10], is shown in Table. 5, where the question marks indicate the parameters (pitch rate, q, elevator deflection, η, and aileron deflection, ξ) which are varied to match the given load factor, n_z, and maximum achievable steady-state roll rate, $p_{\max}$. In this case, the trimming around the pitch axis is performed using the horizontal tailplane (HTP).

Table 5
Trim table with manoeuvres used to compute limit loads. Manoeuvres taken from Pusch et al. [10].

ID	Name	n_z	p	q	η	ξ
M0	Level flight	1	0	0	?	0
M1a	Push-over	−1 g	0	?	?	0
M1b	Pull-up	2.5 g	0	?	?	0
M2a	Roll and push	0	$p_{\max}$	?	?	?
M2b	Roll and pull	$\frac{2}{3} \cdot 2.5$ g	$p_{\max}$	?	?	?

For the determination of C_{defl}, Eq. (7) shows that the main driver behind the downwash value seen by the DLM panels is δ; hence, the movable deflection needs to be limited through a downwash limit.

The downwash constraint C_{defl} limits the effective deflection angles of the flaperon system to prevent unrealistic aerodynamics in DLM. Separate constraints are applied to flap downwash, $w_{j,f}$ and aileron downwash, $w_{j,\text{ail}}$, and their combined effect flaperon downwash, $w_{j,\text{fn}}$. Maximum deflection are set to 45° down for flaps and ± 35° the ailerons. Values which are intentionally higher than typical design ranges [29,49] to account for multi-element high-lift systems that achieve a greater ΔC_L [11,12,29,50] than the plain flap used in the parameterisation framework.

For the implementation of C_p, the regulatory requirements are used. They describe roll performance as the time necessary to accomplish a 60° bank angle reversal [40]. In general, by specifying a $p_{\max}$ of 15 °/s, the handling quality requirements are fulfilled, and is an approach that consistent with prior studies [10,48]. Because actuator dynamics and inertia effects are not explicitly modelled, no additional handling quality constraints are applied.

Finally, to prevent overestimation of the lift performance, due to the absence of flow separation modelling, the angle of attack (AoA) and elevator deflection, η, are limited through C_{AoA}, and C_η, for which the limits are ± 10°, and ± 15° respectively. These limits have been selected, as one can assume attached flow within these values [29].

The feedback coupling between the HQ and MLA optimisation, indicated in Fig. 7, is created by subtracting the downwash distribution, determined inside the HQ optimisation to satisfy the C_p constraint, from $C_{\text{defl.}}$. This step creates $C_{\text{defl., 2}}$, which contains the downwash budgets for MLA. An example of this step is given for a B-spline control point in Eq. (16).

$$-0.4 - \min\left(w_j^{\text{HQ}}\right) \leq w_j^{CP} \leq 0.4 - \max\left(w_j^{\text{HQ}}\right) \tag{16}$$

5. Results

This section presents the results obtained using the optimisation problem described in the previous section. First, the HQ results are presented in Section 5.1, followed by the MLA results in Section 5.2.

5.1. Handling qualities

The HQ analysis is the first step in the optimisation loop, providing constraints to the MLA optimisation. To that end, Eq. (15) is solved for the minimal $M_{\beta,\text{roll}}$ for a fixed geometric parameterisation of the movable region as presented in Table. 3. The design variables available are the $\mathbf{D}_{\text{CP}}$, discussed in Section 2.2.

Figs. 9 and 10 shows the optimised downwash and corresponding lift distribution for five representative flight points. These points have been selected because they represent the low-speed takeoff and approach conditions, the climb-out and descent phases, and the cruise phase. Other flight points listed in Table. 2 exhibit similar trends and are omitted for clarity, as their dynamic pressures are encompassed by the plotted results.

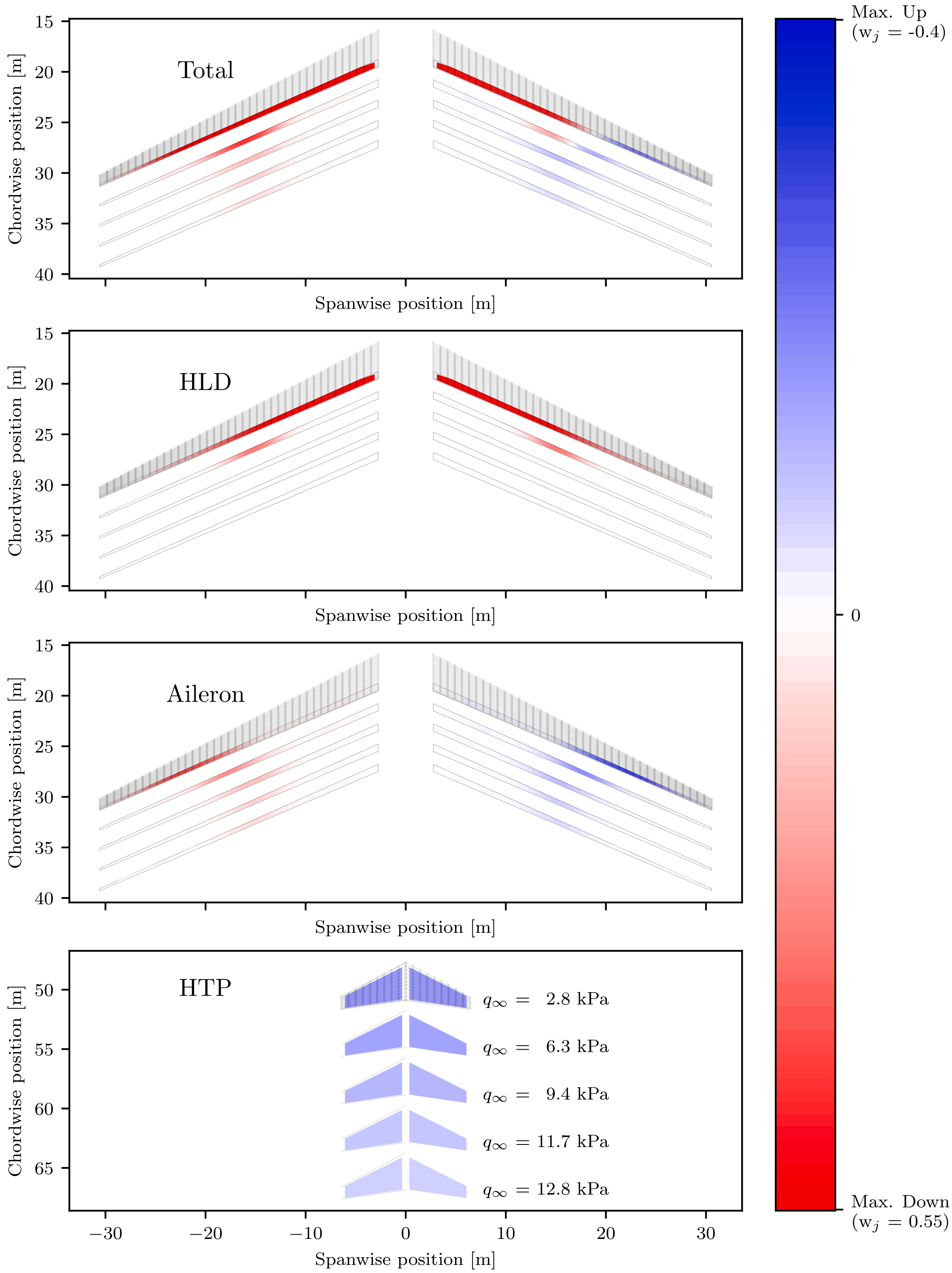

Fig. 9. Downwash distribution for 15°/s right roll at different q_∞. Downwash distributions plotted for the flaperon (Total) and its contributing components. Seen from above.

The downwash distribution in Fig. 9 represents the intended position and deflection of the movables. When a downwash value is plotted in red, the downwash distribution represents a downward deflection, whereas an upward deflection is plotted in blue.

To achieve the 15°/s right roll, a downward downwash is applied to the left wing, whereas an upward downwash is applied to the right wing by the aileron surface. The corresponding lift distribution, plotted in Fig. 10, shows the upward downwash load on the left wing, and the downward downwash load on the right wing. The downwash loads locally increase and decrease the total lift, resulting in the required rolling moment to meet the roll-rate requirements.

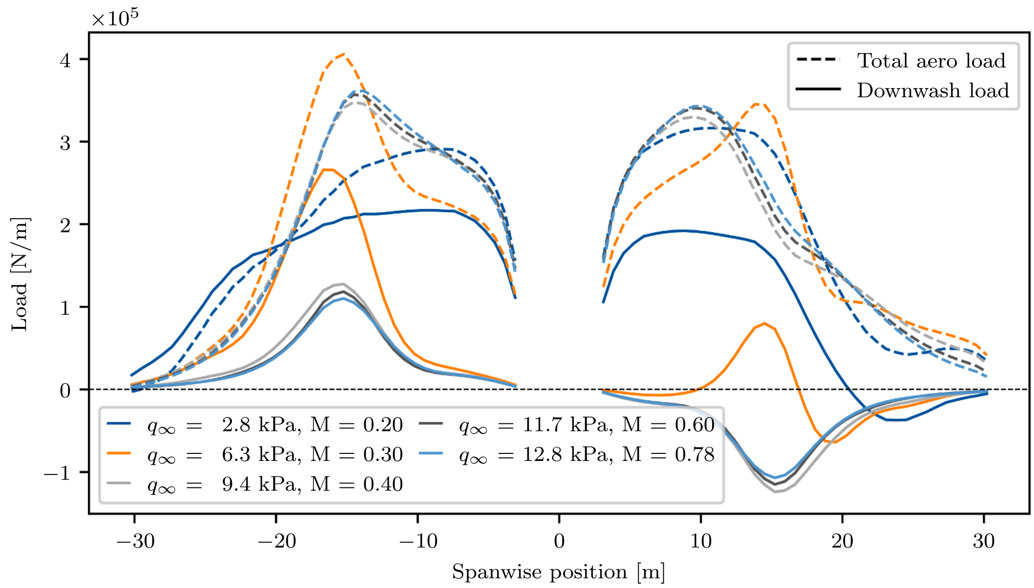

Fig. 10. Spanwise lift distributions for 15 °/s right roll at different q_∞. Solid lines indicate lift distribution generated through downwash application. Dashed lines indicate total lift distribution.

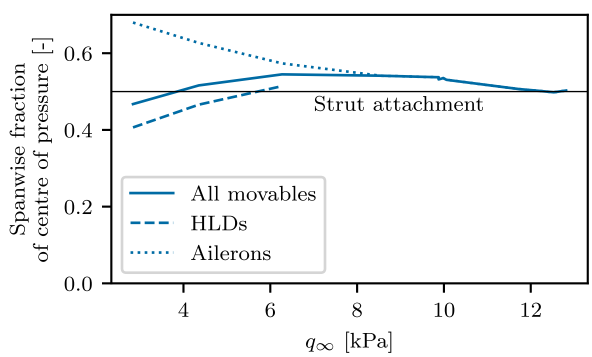

Fig. 11. Spanwise location of centre of pressure during roll for different q_∞.

Besides the roll-rate constraint, the optimiser must also satisfy the trimming constraints C_{AoA} and C_η respectively. First of all, this is achieved through a change in the AoA of the aircraft. However, in case the limits of the C_{AoA} and C_η are reached, the high lift device (HLD) are used, using the method described in Section 2.2. The magnitude of the downwash associated with the HLDs is a design variable in the same way as the aileron downwash. Inspecting the downwash distributions in Fig. 9 or the centre of pressure location in Fig. 11, shows that the HLD downwash is only necessary for a q_∞ of 6.3 kPa or less.

The result in Fig. 9 show that the optimiser placed the HLD downwash in the inboard regions of the wing, even though it had the ability to place it anywhere within the movable region. The reasons for this location are twofold. First of all, the centre of pressure of the ailerons needs to be far enough outboard to generate the required rolling moment to satisfy the C_p constraint. Secondly, due to the use of a constant chord fraction of the movable region, the absolute movable chord is largest in the inboard region, allowing for the largest lift increase.

Comparing the downwash and lift distributions in Figs. 9 and 10, it can be seen that the downwash associated with the ailerons is moving inboard with the increasing dynamic pressure, whereas the downwash corresponding to the HLDs is moving outboard. This behaviour is shown in Fig. 11, which also shows the position of the centre of pressure associated with all movables.

The reason for the movement of the aileron centre of pressure is again twofold. First of all, the moment arm needs to be large enough to generate the required rolling moment. Secondly, the wing outboard of the wing-strut intersection, at 50 % semi-span, is behaving like a very flexible cantilever, as can be seen in Fig. 12. Because of the large flexibility of the outboard region, the control effectiveness of the ailerons is significantly impacted when the q_∞ is increased. The strut-attachment location has the largest torsional stiffness, hence, being able to provide the largest amount of control effectiveness. A similar rationale explains the movement of the HLD toward this region.

Comparing the centre of pressure of the ailerons and HLDs to the centre of pressure of the combined downwash distribution in Fig. 11, it can be seen that the total centre of pressure is centred around the strut attachment location for the whole q_∞ range. At a q_∞ below 4 kPa, the total centre of pressure is driven by the downwash associated with the HLDs, whereas above this q_∞, the aileron downwash is driving. This is in line with expectations, as at the lowest q_∞, the HLDs are generating the largest force. This is caused by their respective chord and applied downwash value. It is also interesting to mention, that for the whole q_∞ range, the centre of pressure associated to all movables is centred around the strut attachment location. This is again caused by the high torsional stiffness in this region, minimising the torsional deformation.

In summary, the position of the aileron and HLD downwash is determined by the required rolling moment, enforced by constraint C_p, as well as the trimming constraints C_{AoA} and C_η. At higher q_∞, HLDs are no longer required for trimming, allowing the aileron downwash to move inboard as the required moment arm decreases.

5.2. *Manoeuvre load alleviation*

In the second step of the optimisation loop, the MLA analysis is performed. By updating the downwash limits using Eq. (16), the effect of the HQ analysis is included in the optimisation.

Fig. 13 shows the optimised downwash and corresponding lift distributions for three representative flight points, which satisfy the C_p constraint and retain a deflection budget for MLA. Other flight points within the q_∞ range exhibit similar behaviour and are omitted for clarity.

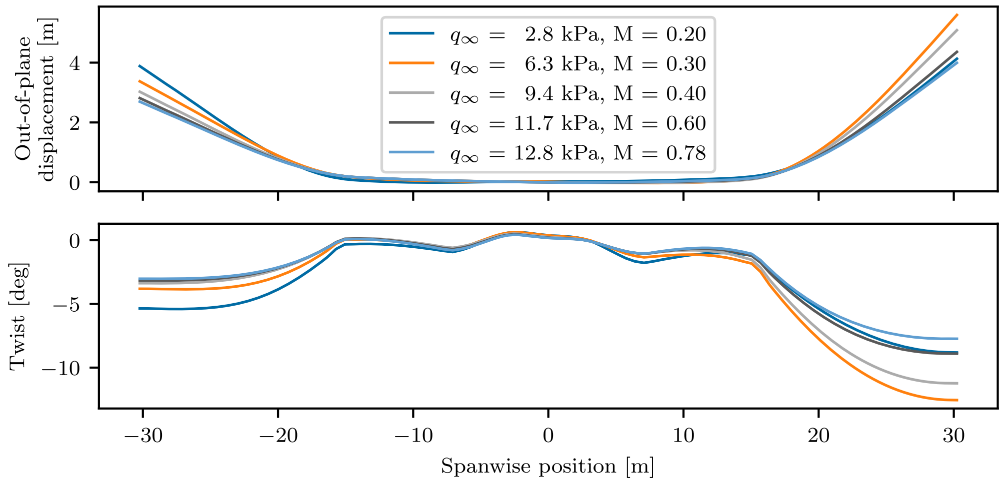

Fig. 12. Deformation of the wing along 50 % c during right roll at different q_∞.

Downward deflection is indicated in red and upward deflection in blue, consistent with the HQ results. Fig. 13b shows the spanwise lift distributions: the dotted line indicates the total aerodynamic load without MLA. The dashed line indicates the total aerodynamic load with MLA, whereas the solid line indicated the aerodynamic load generated by the applied downwash.

Compared to the reference case, total lift decreases outboard of 15 m semi-span and increases in the inboard region. As the aircraft must remain trimmed at the specified load factor, n_z, the integral of the redistributed total lift is equal to the reference lift. As the centre of pressure of the lift redistribution is moving inboard, the moment arm is reduced, which in turn reduces the applied RBM. To achieve the lift redistribution, an upward downwash is applied in the outboard region, while a downward downwash is applied in the inboard region, as is illustrated in Fig. 13.

Inspecting Fig. 13a, it can be seen that the downwash applied by the optimiser is at its respective positive and negative limits. This behaviour is expected, as the optimiser maximises the inboard movement of the centre of pressure, hence, achieving the greatest impact on the lift distribution. This behaviour has also been observed by Kier [51].

Furthermore, Fig. 13a shows that even though the continuous movable parameterisation allows a chordwise downwash variation, which can be achieved using a morphing movable, the optimiser did not use this ability during the optimisation process. The lack of chordwise downwash variation is due to the large sweep of the wing. Hence, the effect on the total lift distribution of the chordwise variation in downwash along the c_{mov} of 20 % c is small compared to the effect of the spanwise downwash variation, and hence, the spanwise downwash variation is preferred.

Another phenomenon in Fig. 13a is that increasing q_∞ moves the split between positive and upward downwash inboard and adds downward downwash near the wing tip. Although downward downwash is applied at the tip to increase local lift (see Fig. 13b), a negative downwash load is used.

To investigate the appearance of the positive downwash in the tip region, and determine if control reversal is present in the tip region, the change in total lift due to a change in downwash at a single downwash control point is investigated for q_∞ = 12.8 kPa and n_z = 2.5 g. Within this investigation the definition of control reversal is the reduction of total lift, when a positive (downward) deflection/downwash is applied. The starting point of the investigation are a clean wing which is experiencing the aforementioned flight conditions. The results are shown in Fig. 14, which shows the total lift variation due to a local downwash increase of 0.1 for a rigid and flexible aircraft in Fig. 14a, and the corresponding control effectiveness, ε, distribution in Fig. 14b. In Fig. 14a, both the rigid and flexible aircraft results show that the closer one gets to the tip, the smaller the change in total lift is. This behaviour is as expected, as the movable area reduces towards the tip, as a constant c_{mov} is used.

Investigating the difference between the flexible and rigid aircraft results, indicated in blue in Fig. 14a, shows that the difference up to 50 percent semi-span remains constant. This is in line with expectations, as this region is supported between the wing root and the wing-strut intersection and therefore has a large torsional stiffness. Outboard of 50 % semi-span, the difference is increasing, which is caused by the washout behaviour of the cantilever wing section. The largest difference is found in the 22 m to 31 m region, where the flexible aircraft also experiences a reduction in total lift. Because of the reduction of total lift in the outboard region, it can be concluded that this region is operating in the control reversal regime.

To further support, the statement that the optimiser is actively exploiting control reversal, the ε is determined using the following equation:

$$\varepsilon = \frac{\left(\frac{\partial L}{\partial \mathrm{w}_j}\right)_{\text{flex}}}{\left(\frac{\partial L}{\partial \mathrm{w}_j}\right)_{\text{rigid}}}. \tag{17}$$

The spanwise variation of ε is shown in Fig. 14b. It can be seen that in the 10 m to 15 m semi-span range, the value of ε is increasing, which is explained by the larger torsional stiffness of the wing due to the wing-strut attachment in this location. Furthermore, in the 22 m to 31 m semi-span region, it can be seen that the ε is negative. Hence, this region is experiencing control reversal, which the optimiser is actively exploiting.

To further investigate the spanwise variation of the downwash distribution, as well as the increase in total lift in the tip region, the MLA optimisation has been performed on a movable region where y_2 is changed to 85 % semi-span with no changes to the other movable region parameters. The results for this optimisation are shown in Fig. 15, with Table. 6 comparing the amount of RBM reduction which can be achieved. In the table, "Partial TE" indicates the movable region with $y_2 = 85\,\%$ semi-span, whereas "Full TE" indicates the movable region with $y_2 = 100\,\%$ semi-span.

The behaviour shown in Fig. 15 is similar to the behaviour shown by the full TE in Fig. 13. However, it is interesting to note that downward downwash does not appear in the tip region. Hence, it can be concluded

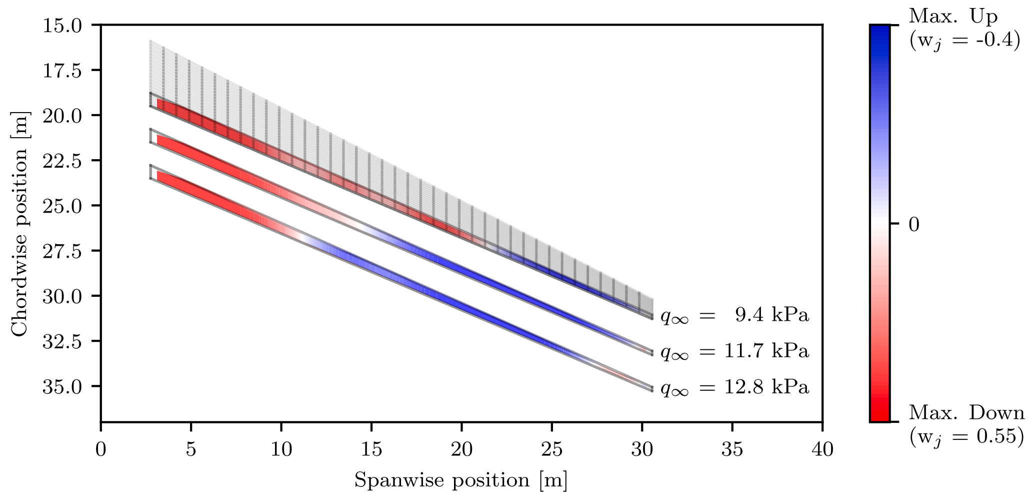

(a) Downwash distribution for MLA at different q_∞.

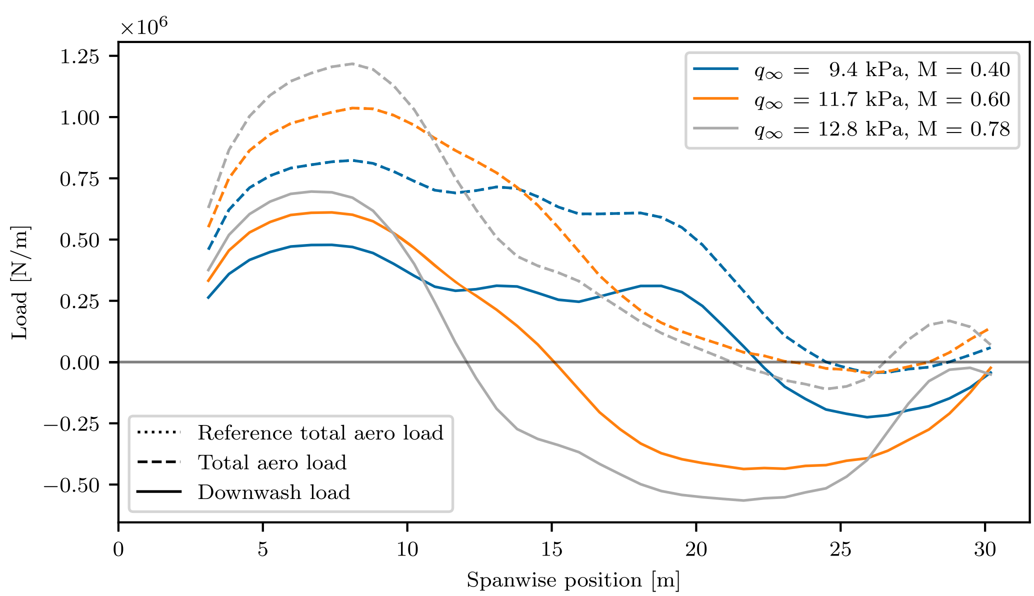

(b) Spanwise lift distribution for MLA at different q_∞.

Fig. 13. Downwash and spanwise lift distribution for MLA at different q_∞.

Table 6
RBM reduction for different dynamic pressures.

q_∞ [kPa]	Full TE [%]	Partial TE [%]
9.4	7.6	8.5
11.7	23.6	23.4
12.8	30.5	29.1

that in this case the wing is not experiencing control reversal. This is supported by the fact that the reduction in total lift, shown in Fig. 15, is achieved using an upward downwash load.

Comparing the lift distributions in Figs. 13b and 15b, it can be seen that for the lowest q_∞, at 9.4 kPa, the centre of pressure is actually further inboard for the partial TE than for the full TE, which results in the larger RBM reduction for the partial TE shown in Table. 6. For the higher q_∞, the larger span of the TE movable allows for a larger RBM reduction.

The observed differences are caused by the wing's flexibility, with the control effectiveness in the tip region, outboard of 85 % semi-span being small or even negative for certain flight conditions. This can be concluded from the out-of-plane and twist deformation presented in Fig. 16, which shows large deformations for both the reference and MLA case. Comparing the deformations for full and partial TE, it can be seen that both the out-of-plane and twist deformations show different behaviours from 25 m semi-span. Comparing the displacements, it can be seen that for the full TE, the movables are able to reduce the deformations; however, the order of magnitude and shape of both deformations are similar for the full and partial TE results. Hence, the movables outboard of 15 % semi-span cannot provide a larger amount of RBM reduction, causing the difference to vary between 0.1 to 1.4 percentage points as seen in Table. 6.

To conclude on the MLA results, the behaviour of the optimised downwash distribution is driven by the reduction of the RBM, which drives the centre of pressure inboard as far as possible, while the C_{AoA} and C_η constraints limit this movement. For the full TE case, this meant

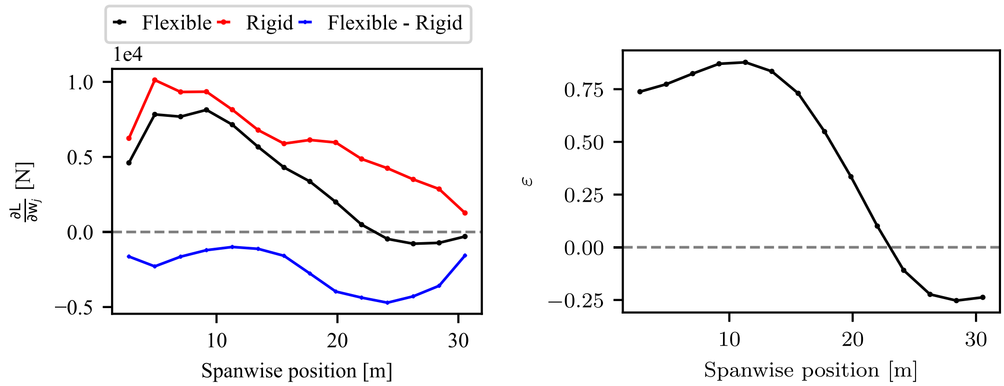

(a) Total lift variation for a local downwash variation of 0.1 for the flexible (black) and rigid (red) aircraft. The difference in total lift variation between the flexible and rigid aircraft is shown in blue.

(b) Comparison of the control effectiveness, ε, along the span

Fig. 14. Spanwise distribution of total lift variation due to a change in downwash, and corresponding control effectiveness distribution at q_∞ = 12.8 kPa and n_z = 2.5 g.

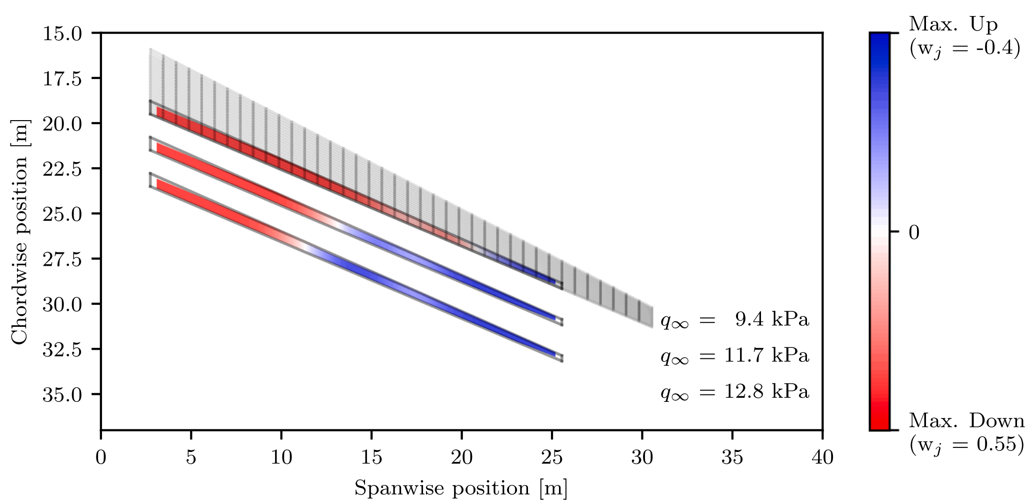

(a) Downwash distribution for MLA at different q_∞. Movable region from 0 % to 85 % semi-span.

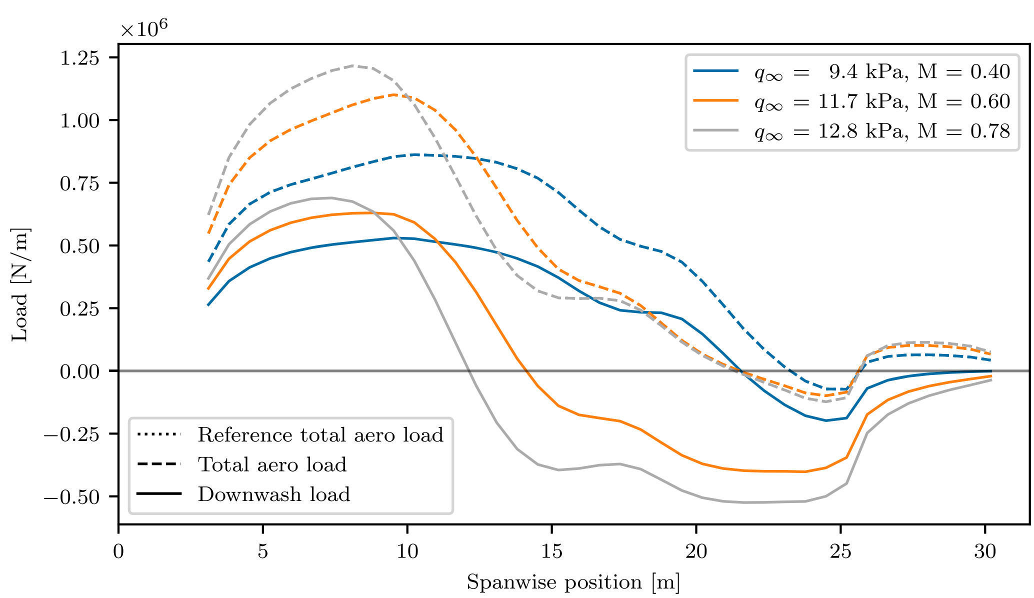

(b) Spanwise lift distribution for MLA at different q_∞. Movable region from 0 % to 85 % semi-span.

Fig. 15. Downwash and spanwise lift distribution for MLA at different q_∞. Movable region from 0 % to 85 % semi-span.

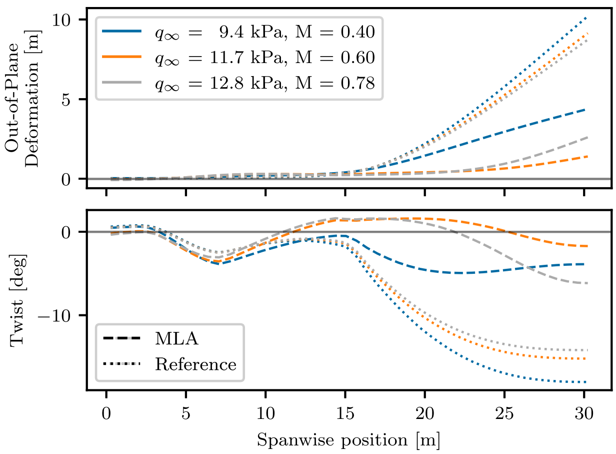

(a) Deformations along 50 % chord. Full TE.

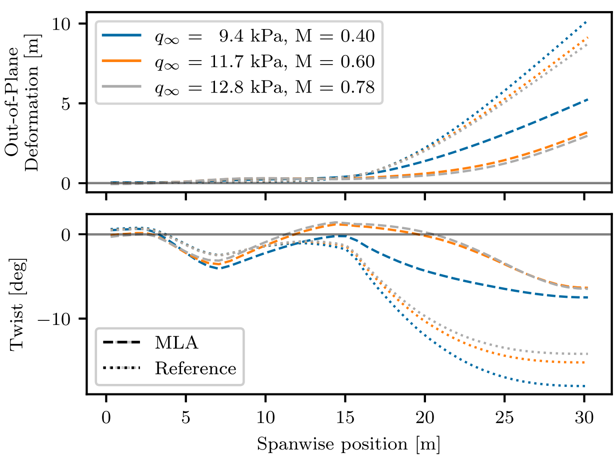

(b) Deformations along 50 % chord. Partial TE.

Fig. 16. Deformations along 50 % chord.

that the outer sections of the wing where experiencing control reversal. For the partial TE, the wing had enough torsional stiffness to prevent the occurance of control reversal. Furthermore, although the framework allows for chordwise variation of downwash, the optimiser did not utilise this capability. This is because of the large sweep of the wing and the 20 % c of the movables, which causes the effect on the lift distribution of the chordwise variation in downwash to be small compared to the spanwise variation; hence, a spanwise variation in downwash is preferred. Finally, comparing the RBM reduction for the full and partial TE movable regions, it can be seen that the differences between the two optimised downwash surfaces are equal to or less than 1.4 percentage points. The small differences are caused by the wing's flexibility, with the outboard region having low control effectiveness; hence, it makes a negligible contribution to the RBM reduction.

6. Conclusion and outlook

The work presented in this paper introduced a novel methodology for continuous parameterisation of movables, which uses direct assignment of the downwash to the doublet lattice method (DLM) panels to model the movable layout. The parameterisation has been applied to a high aspect ratio strut-braced wing aircraft to demonstrate the capability of the framework.

The results presented in this paper demonstrate the successful application of the continuous parameterisation. They demonstrate the ability of the parameterisation to be applied to an aircraft for which only the planform and initial structural parameters are known, allowing it to be used to explore the optimal positions of the movables.

Several notable results were observed. First of all, the optimal downwash distribution for handling qualities (HQ) and manoeuvre load alleviation (MLA) changes with free-stream dynamic pressure, q_∞. For this aircraft model, the movable position required for HQs are driven by the required amount of high lift device (HLD) downwash, to ensure the aircraft remains trimmed, combined with the required moment arm generated by the aileron downwash. As q_∞ is increased, the centre-of-pressure for both the HLD and ailerons downwash shifted toward 50 % semi-span due to increased torsional stiffness at the strut attachment, enhancing control effectiveness in this region.

For the MLA results, an interesting phenomenon is that the optimiser has not used the ability of varying the downwash in the chordwise direction. Due to the large sweep of the wing, the chordwise variation in downwash is small compared to the spanwise variation. Hence, to reduce the root bending moment (RBM) as much as possible, a spanwise variation of downwash is preferred to meet all the specified constraints.

The effect of reducing the spanwise extent of the movable regions was evaluated by changing spanwise stop position, y_2, to 85 % semi-span (Partial trailing edge (TE)). It was found that for the current aircraft, the differences in RBM reduction between the movable region along the full and partial TE were less than or equal to 1.4 percentage points, indicating that the additional effect of the outer 15 % semi-span contributes negligibly to RBM reduction due to wing flexibility.

Overall, these results demonstrate the versatility of the continuous movable parameterisation framework, which can be applied to a given wing planform with specified structural parameters while allowing user-defined positional constraints.

Both the HQ and MLA results were obtained using a 1:1 weighting factor between the RBM reduction and the total hinge moment, $M_{\beta,\mathrm{all}}$. However, different weighting factors for the two objectives may result in different movable layouts. Hence, when applying the presented parameterisation methodology to an aircraft for which the movable layout needs to be determined, a trade-off study between the different objectives must be performed.

Furthermore, currently it is assumed that the chordwise downwash distribution can be modelled using the methodology presented in this paper. However, this assumption requires the implementation of constraints on the values inside the downwash vector, $\mathbf{w}_j$. To validate the constraint values, future work will require the comparison of the achievable complex differential pressure coefficient, $\Delta\mathbf{c}_\mathrm{p}$, using the B-spline downwash distribution, with the $\Delta\mathbf{c}_\mathrm{p}$ that can be modelled using a higher fidelity method that can capture flow separation, to determine if the corresponding aerofoil shape is physically representable. One way to do this, would be to perform an inverse design process using the DLM $\Delta\mathbf{c}_\mathrm{p}$ within a higher fidelity method, for example a Reynolds-averaged Navier-Stokes (RANS) solver.

Besides the aforementioned points, future work will extend the framework to unsteady analyses, such as gust encounters. This will allow for the consideration of gust load alleviation (GLA) during the optimisation of the movable layout. Furthermore, coupling HQ, MLA, and GLA in a single optimisation loop would enable the study of combined manoeuvres and gust effects on aircraft loads. Furthermore, the effect of different types of unconventional aircraft, such as Prandtl-Planes (PrPs), can be investigated. Furthermore, the results presented are determined using linear aerodynamics, which generally overestimate the performance that can be obtained. Hence, including a higher-fidelity aerodynamics method through a hybrid analysis combining DLM with computational fluid dynamics (CFD) data is expected to improve the performance estimates obtained using the presented framework.

Disclaimer

Co-Funded by the European Union. Views and opinions expressed are, however, those of the authors only and do not necessarily reflect those of the European Union or Clean Aviation Joint Undertaking. Neither the European Union nor the granting authority can be held responsible for them.

Declaration of generative AI and AI-assisted technologies in the manuscript preparation process

Artificial intelligence (AI) was utilised in the writing process to assist with language refinement and clarity. All AI-generated content was reviewed and verified by the authors to ensure accuracy and alignment with the research objectives.

CRediT authorship contribution statement

Stefan de Boer: Conceptualization, Methodology, Software, Writing – original draft, Writing – review & editing, Visualization; **Roeland De Breuker:** Writing – review & editing, Supervision, Funding acquisition; **Jurij Sodja:** Writing – review & editing, Supervision, Funding acquisition.

Declaration of competing interest

The authors declare that they have no known competing financial interests or personal relationships that could have appeared to influence the work reported in this paper.

Acknowledgement

The work presented herein has been partially funded by the European Community's Clean Aviation programme under Grant Agreement 101101974. The UPWing project (Ultra-Performance Wing) is funded under Climate, Energy and Mobility and involves 26 partners. The project started on January 1, 2023. The aircraft model is an evolution of the baseline configuration in the UPWing project. The authors would like to thank Charly Mollet and Lander Vertonghen from ONERA-MSAE/MC2 for providing the aircraft model. Furthermore, the authors would like to thank Eric Nguyen Van and Sebastien Defoort from ONERA-DTIS for providing the aircraft mission from which the flight points have been extracted.

CLEAN AVIATION Co-funded by the European Union

Data availability

Data will be made available on request.

References

[1] D. Reckzeh, Multifunctional wing movables: design of the A350XWB and the way to future concepts, in: 29th Congress of the International Council of the Aeronautical Sciences (ICAS), St. Petersburg, 2014.

[2] D. Sanghi, C. Riso, C.E. Cesnik, F. Vetrano, Impact of control-surface flexibility on the dynamic response of flexible aircraft, in: AIAA Scitech 2020 Forum, AIAA SciTech Forum, American Institute of Aeronautics and Astronautics, 2020. https://doi.org/10.2514/6.2020-1185

[3] D. Sanghi, C. Riso, C. Cesnik, F. Vetrano, Influence of aileron placement on roll response of high-aspect-ratio-wing aircraft, in: AIAA AVIATION 2020 FORUM, AIAA AVIATION Forum, American Institute of Aeronautics and Astronautics, 2020. https://doi.org/10.2514/6.2020-2645

[4] D. Sanghi, Maneuverability, Load Alleviation, and Ride Qualities of Transonic High-Aspect-Ratio-Wing Aircraft, Ph.D. thesis, University of Michigan, 2022. https://doi.org/10.7302/6868

[5] T.F. Wunderlich, F. Siebert, Optimization of control surface deflections on the high aspect ratio wing to improve cruise flight performance, in: New Results in Numerical and Experimental Fluid Mechanics XIV, Notes on Numerical Fluid Mechanics and Multidisciplinary Design, Springer Nature Switzerland, Cham, 2022, pp. 206–215. https://doi.org/10.1007/978-3-031-40482-5_20

[6] C. Riso, D. Sanghi, C.E. Cesnik, F. Vetrano, P. Teufel, Parametric roll maneuverability analysis of a high-aspect-ratio-wing civil transport aircraft, in: AIAA Scitech 2020 Forum, AIAA SciTech Forum, American Institute of Aeronautics and Astronautics, 2020. https://doi.org/10.2514/6.2020-1191

[7] Y. Ma, M. Abouhamzeh, A. Elham, Aerostructural optimization and comparative study of strut-braced-wing and twin-fuselage aircraft configurations with ultra-high aspect ratio wings, in: AIAA SCITECH 2023 Forum, AIAA SciTech Forum, American Institute of Aeronautics and Astronautics, 2023. https://doi.org/10.2514/6.2023-2204

[8] D. Muradas Odriozola, S. Marquier, J. Morlier, C. Gogu, A preliminary low-fidelity MDO approach for load alleviation through movables on HAR wing, in: Aerobest 2023, ECCOMAS, Portugal, Lisboa, Portugal, 2023.

[9] D. Muradas Odriozola, S. Marquier, J. Morlier, C. Gogu, Control surface sizing and design through integrated MDO approach: enhancing load alleviation while preserving handling quality criteria, in: Aeroelasticity & Structural Dynamics in a Fast Changing World, Den Haag, the Netherlands, 2024.

[10] M. Pusch, A. Knoblach, T. Kier, Integrated optimization of control surface layout for gust load alleviation, CEAS Aeronaut. J. 10 (4) (2019) 1059–1069. https://doi.org/10.1007/s13272-019-00367-4

[11] D. Reckzeh, Aerodynamic design of the high-lift-wing for a megaliner aircraft, Aerosp. Sci. Technol. 7 (2) (2003) 107–119. https://doi.org/10.1016/S1270-9638(02)00002-0

[12] H. Strüber, The aerodynamic design of the A350 XWB-900 high lift system, in: 29th Congress of the International Council of the Aeronautical Sciences, St. Petersburg, 2014.

[13] V. Handojo, P. Lancelot, R. De Breuker, Implementation of active and passive load alleviation methods on a generic mid-range aircraft configuration, in: 2018 Multidisciplinary Analysis and Optimization Conference, AIAA AVIATION Forum, American Institute of Aeronautics and Astronautics, 2018. https://doi.org/10.2514/6.2018-3573

[14] V. Handojo, J. Himisch, K. Bramsiepe, W.R. Krüger, L. Tichy, Potential estimation of load alleviation and future technologies in reducing aircraft structural mass, Aerospace 9 (8) (2022) 412. https://doi.org/10.3390/aerospace9080412

[15] V. Handojo, S. Pülm, Potential limits of load alleviation in reducing the structural mass of a long-range transport configuration, in: 34th Congress of the International Council of the Aeronautical Sciences (ICAS), Florence, Italy, 2024.

[16] S. Binder, A. Wildschek, R. De Breuker, The interaction between active aeroelastic control and structural tailoring in aeroservoelastic wing design, Aerosp. Sci. Technol. 110 (2021) 106516. https://doi.org/10.1016/j.ast.2021.106516

[17] G.E. Bona, K. Risse, A functional approach to a collaborative iintegrated wing and movables design, in: 2018 AIAA Aerospace Sciences Meeting, AIAA SciTech Forum, American Institute of Aeronautics and Astronautics, Kissimmee, Florida, 2018. https://doi.org/10.2514/6.2018-2031

[18] T.A. Weisshaar, Morphing aircraft systems: historical perspectives and future challenges, J. Aircr. 50 (2) (2013) 337–353. https://doi.org/10.2514/1.C031456

[19] T. Mkhoyan, Autonomous Smart Morphing Wing: Development, Realisation & Validation, Ph.D. thesis, Delft University of Technology, 2022.

[20] T. Mkhoyan, N.R. Thakrar, R. De Breuker, J. Sodja, Design and development of a seamless smart morphing wing using distributed trailing edge camber morphing for active control, in: AIAA Scitech 2021 Forum, AIAA SciTech Forum, American Institute of Aeronautics and Astronautics, 2021. https://doi.org/10.2514/6.2021-0477

[21] N. Nguyen, U. Kaul, S. Lebofsky, E. Ting, D. Chaparro, J. Urnes, Development of variable camber continuous trailing edge flap for performance adaptive aeroelastic wing, in: SAE AeroTech Congress & Exhibition, Seattle, WA, 2015.

[22] N.T. Nguyen, E. Ting, D. Chaparro, M.C. Drew, S.S.-M. Swei, Multi-objective flight control for drag minimization and load alleviation of high-aspect ratio flexible wing aircraft, in: 58th AIAA/ASCE/AHS/ASC Structures, Structural Dynamics, and Materials Conference, AIAA SciTech Forum, American Institute of Aeronautics and Astronautics, Grapevine, Texas, 2017. https://doi.org/10.2514/6.2017-1589

[23] B.K. Stanford, Static and dynamic aeroelastic tailoring with variable-camber control, J. Guid. Contr. Dyn. 39 (11) (2016) 2522–2534. https://doi.org/10.2514/1.G000413

[24] R. De Breuker, T. Mkhoyan, N. Nazeer, V. Stuber, X. Wang, I. Mkhoyan, R. Groves, S. van der Zwaag, J. Sodja, Overview of the SmartX wing technology integrator, Actuators 11 (10) (2022) 302. https://doi.org/10.3390/act11100302

[25] N. Werter, J. Sodja, G. Spirlet, R. De Breuker, Design and experiments of a warp induced camber and twist morphing leading and trailing edge device, in: 24th AIAA/AHS Adaptive Structures Conference, AIAA SciTech Forum, American Institute of Aeronautics and Astronautics, San Diego, California, 2016. https://doi.org/10.2514/6.2016-0315

[26] B.K. Stanford, Optimal control surface layout for an aeroservoelastic wingbox, AIAA J. 55 (12) (2017) 4347–4356. https://doi.org/10.2514/1.J056070

[27] B.K. Stanford, Optimal aircraft control surface layouts for maneuver and gust load alleviation, in: AIAA Scitech 2020 Forum, AIAA SciTech Forum, American Institute of Aeronautics and Astronautics, 2020. https://doi.org/10.2514/6.2020-0448

[28] N.F.M. Wahler, Y. Ma, A. Elham, Conceptual design and aerostructural trade-offs in hydrogen- powered strut-braced wing aircraft: insights into dry and wet ultra-high aspect ratio wings, Aerospace 12 (2) (2025) 77. https://doi.org/10.3390/aerospace12020077

[29] E. Torenbeek, Synthesis of Subsonic Airplane Design, Springer Netherlands, Dordrecht, 1982. https://doi.org/10.1007/978-94-017-3202-4

[30] Aircraft Design a Conceptual Approach, AIAA Education Series, American Institute of Aeronautics and Astronautics, Inc, Reston, VA, Sixth edition, 2018.
[31] N.P.M. Werter, R. De Breuker, M.M. Abdalla, Continuous-time state-space unsteady aerodynamic modeling for efficient loads analysis, AIAA J. 56 (3) (2018) 905–916. https://doi.org/10.2514/1.J056068
[32] N.P.M. Werter, Aeroelastic Modelling and Design of Aeroelastically Tailored and Morphing Wings, Ph.D. thesis, Delft University of Technology, 2017.
[33] A. Voß, An Implementation of the Vortex Lattice and the Doublet Lattice Method, Technical Report DLR-IB-AE-GO-2020-137, Institut für Aeroelastik, Deutsches Zentrum für Luft- und Raumfahrt, Göttingen, Germany, 2020.
[34] X. Bertrand, Modélisation aérodynamique des surfaces de contrôle de la voilure d'un avion de transport, Ph.D. thesis, ISAE, Toulouse, 2008.
[35] P. Lancelot, R. De Breuker, Effect of improved flight and control loads modelling on wing-box preliminary sizing:, in: 6th Aircraft Structural Design Conference, Bristol, United Kingdom, 2018.
[36] T. Kier, G. Looye, Unifying manoeuvre and gust loads analysis, in: IFASD 2009, Seattle, USA, 2009.
[37] A. Voß, Loads Kernel User Guide, Version 1.01, Technical Report DLR-IB-AE-GO-2020-136, Institut für Aeroelastik, Deutsches Zentrum für Luft- und Raumfahrt, Göttingen, Germany, 2021.
[38] E. Albano, W.P. Rodden, A doublet-lattice method for calculating lift distributions on oscillating surfaces in subsonic flows, AIAA J. 7 (2) (1969) 279–285. https://doi.org/10.2514/3.5086
[39] J. Katz, A. Plotkin, Low-Speed Aerodynamics, Cambridge Aerospace Series, Cambridge University Press, Cambridge, 2 edition, 2001. https://doi.org/10.1017/CBO9780511810329
[40] CS-25 Amendment 28 | EASA, 2023, (https://www.easa.europa.eu/en/document-library/certification-specifications/cs-25-amendment-28).
[41] N. Werter, R.D. Breuker, A framework for the aeroelastic analysis and design of generic morphing wings, in: 23rd AIAA/AHS Adaptive Structures Conference, American Institute of Aeronautics and Astronautics, Kissimmee, Florida, USA, https://doi.org/10.2514/6.2015-0268
[42] L. Piegl, W. Tiller, The NURBS Book, Monographs in Visual Communication, Springer Berlin Heidelberg, Berlin, Heidelberg, 1997. https://doi.org/10.1007/978-3-642-59223-2
[43] R. De Breuker, N. Werter, On the importance of morphing deformation scheduling for actuation force and energy, Aerospace 3 (4) (2016) 41. https://doi.org/10.3390/aerospace3040041
[44] A.B. Lambe, J.R.R.A. Martins, Extensions to the design structure matrix for the description of multidisciplinary design, analysis, and optimization processes, Struct. Multidiscip. Optim. 46 (2) (2012) 273–284. https://doi.org/10.1007/s00158-012-0763-y
[45] J.S. Gray, J.T. Hwang, J.R.R.A. Martins, K.T. Moore, B.A. Naylor, OpenMDAO: an open-source framework for multidisciplinary design, analysis, and optimization, Struct. Multidiscip. Optim. 59 (4) (2019) 1075–1104. https://doi.org/10.1007/s00158-019-02211-z
[46] O.R. Bingol, A. Krishnamurthy, NURBS-Python: An open-source object-oriented NURBS modeling framework in Python, SoftwareX 9 (2019) 85–94. https://doi.org/10.1016/j.softx.2018.12.005
[47] M. Méheut, D.L. Costoso, F. Moens, O. Atinault, C. Julien, L. Vertonghen, V. Priasso, A. Lannoo, S. Defoort, E.N. Van, C. David, D. Glenis, S. de Boer, J. Schwingel, D. Eisenhut, Strut-braced dry wing concept for hydrogen-powered aircraft, in: 34th Congress of the International Council of the Aeronautical Sciences (ICAS), Florence, Italy, 2024.
[48] M.H. Sadraey, Aircraft Design: A Systems Engineering Approach, Aerospace Series (Chichester, England), Wiley, Hoboken, New Jersey, 2012.
[49] J. Roskam, Airplane Design VII: Determination of Stability, Control and Performance Characteristics: FAR and Military Requirements, DARcorporation, 1985.
[50] C.P. van Dam, The aerodynamic design of multi-element high-lift systems for transport airplanes, Prog. Aerosp. Sci. 38 (2) (2002) 101–144. https://doi.org/10.1016/S0376-0421(02)00002-7
[51] T. Kier, An integrated flexible aircraft model for optimal control surface scheduling of manoeuvre load alleviation and wing shape control functions, in: 19th International Forum on Aeroelasticity and Structural Dynamics, IFASD 2022, Madrid, Spain, 2022.